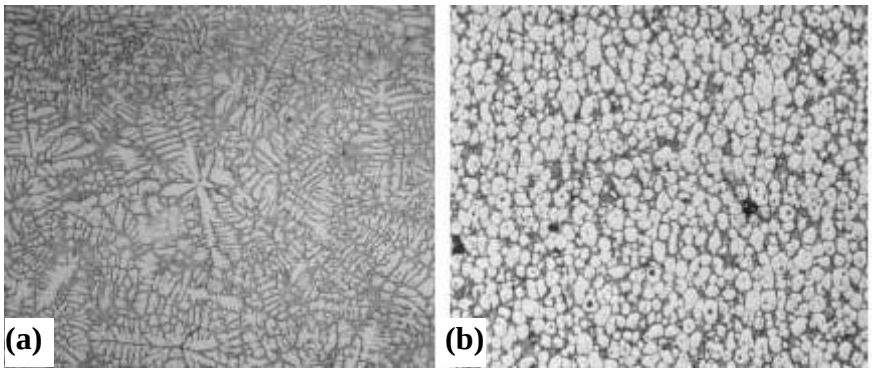

Fig. 1 Micrograph of a typical (a) dendritic microstructure in an as-cast sample and (b) globular microstructure in a semisolid alloy sample.

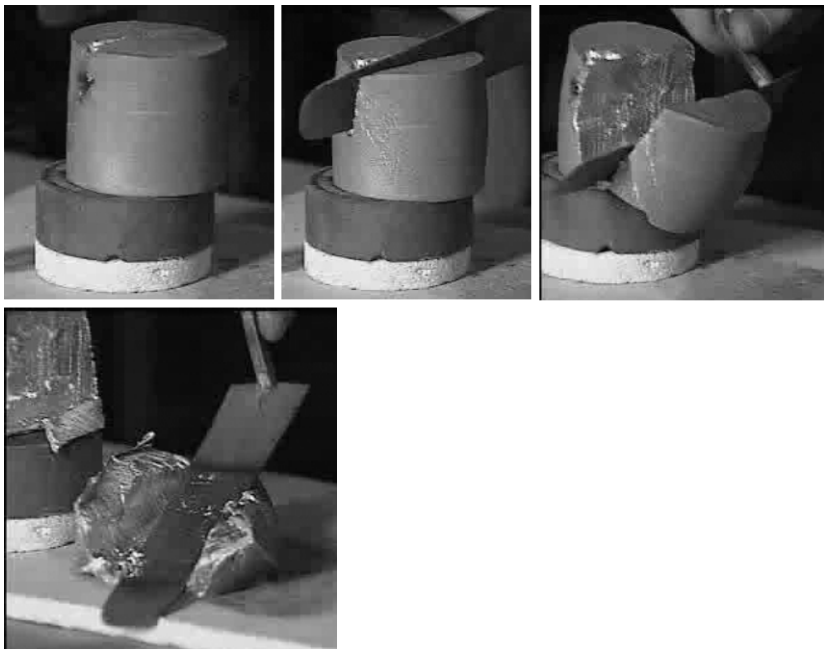

Fig. 2 A photographic sequence illustrating the thixotropic behaviour of semisolid alloy slugs (courtesy University of Sheffield)

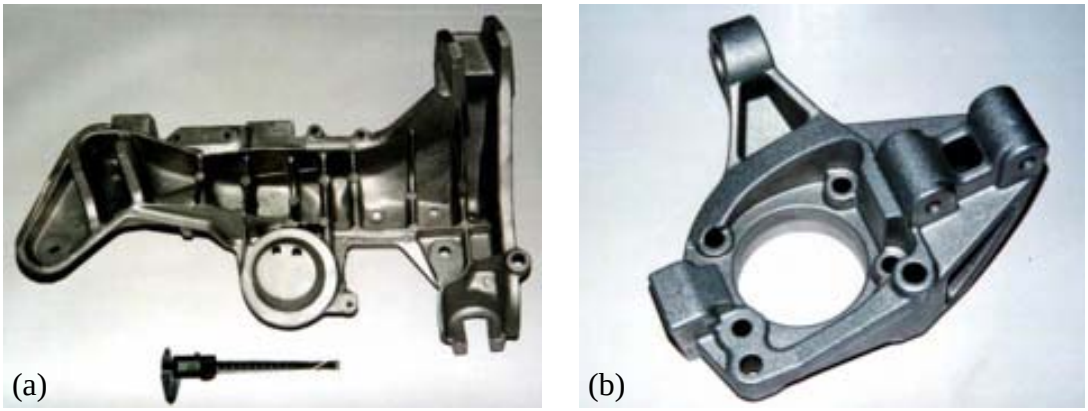

Fig. 3 Automotive components produced by STAMPAL for the Alfa Romeo car

(a) Multi-link, rear suspension support 8.5kg, A357, T5;

(b) Steering knuckle A357, T5 substitution of cast iron part.

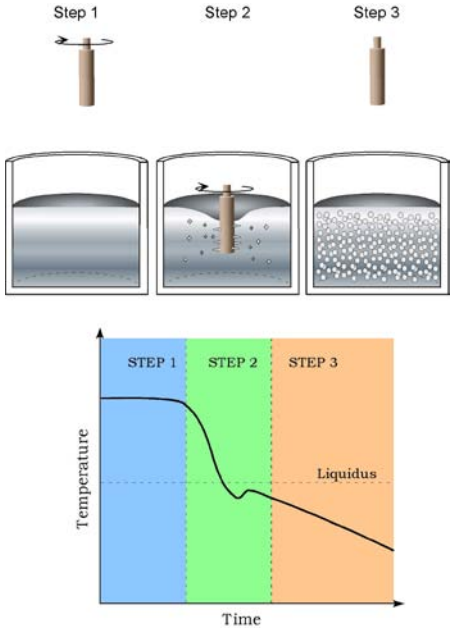

Fig. 4 “New MIT” process (courtesy Prof. M. C. Flemings, MIT)

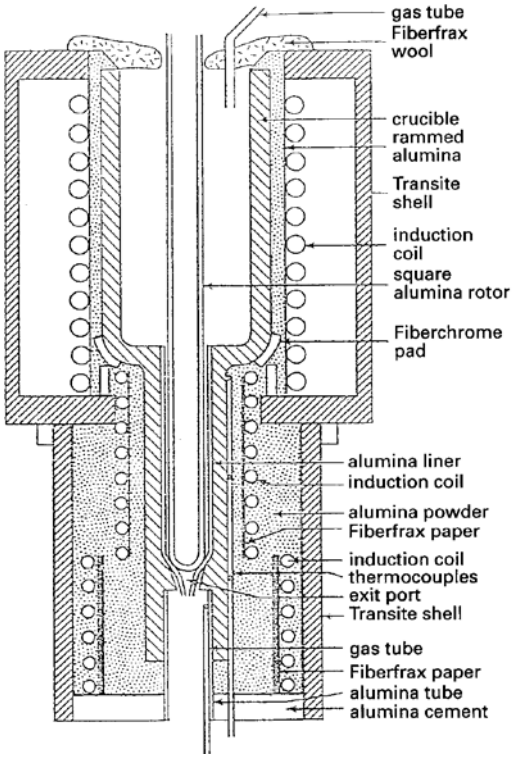

Fig. 5 Continuous rheocaster (after [29])

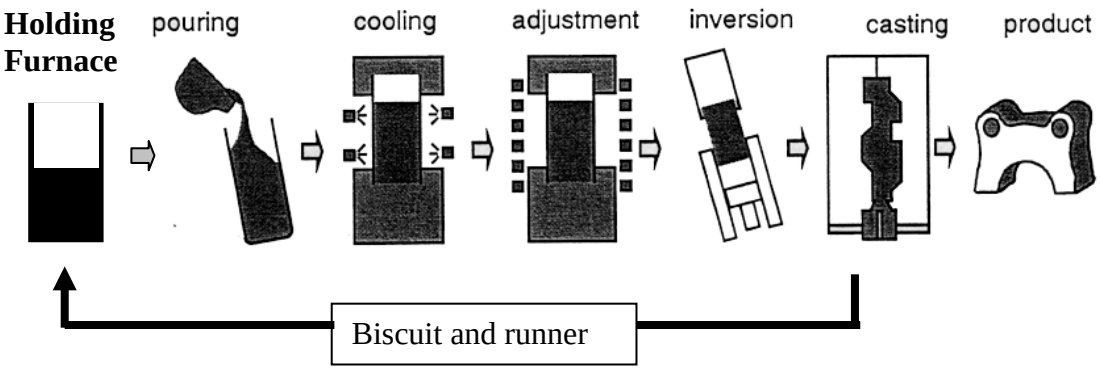

Fig. 6 Schematic diagram of the New Rheocasting (NRC) process. The inversion procedure causes the oxide skin on the exposed surface to run into the runner and biscuit.

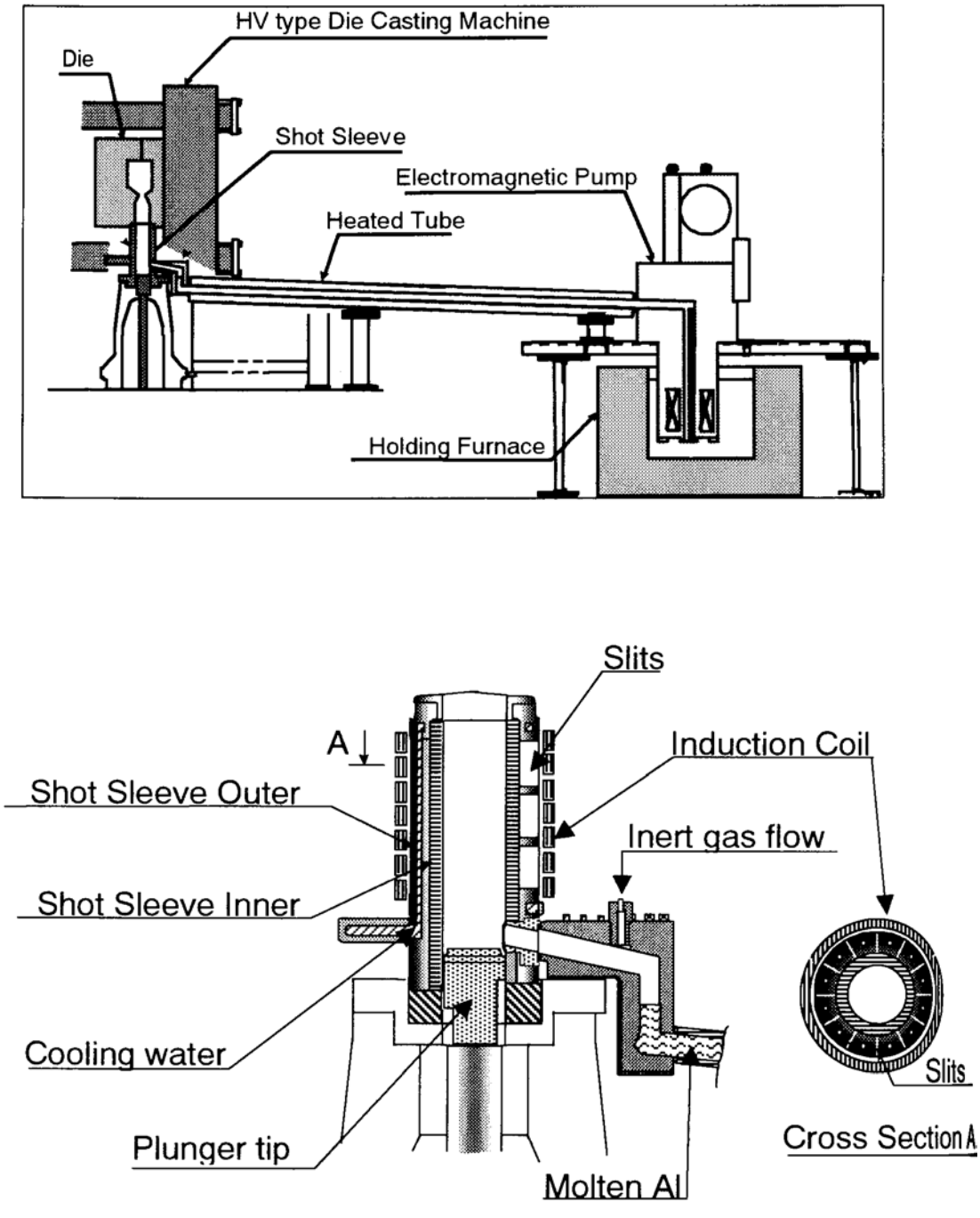

Fig. 7 Electromagnetic stirring in the shot sleeve in the New Semi-Solid Metal Casting process from Hitachi (after [30]).

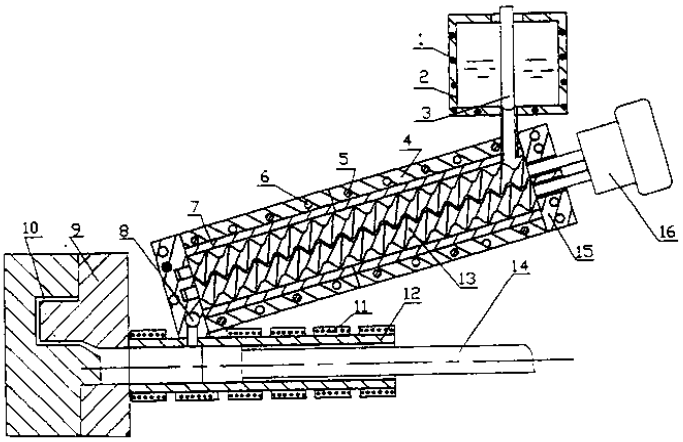

1, Heating elements; 2, crucible; 3, stopping rod; 4, barrel; 5, heating elements; 6, cooling channels; 7, barrel liner; 8, transfer valve; 9, die; 10, mould cavity; 11, heating elements; 12, shot sleeve; 13, twin-screw; 14, piston; 15, end cup; 16, driving system.

Fig. 8 Schematic diagram of a Rheomolder using a twin screw process [34]. Liquid metal is used instead of the solid chips used in the Thixomolder^{TM} (see Fig. 9)

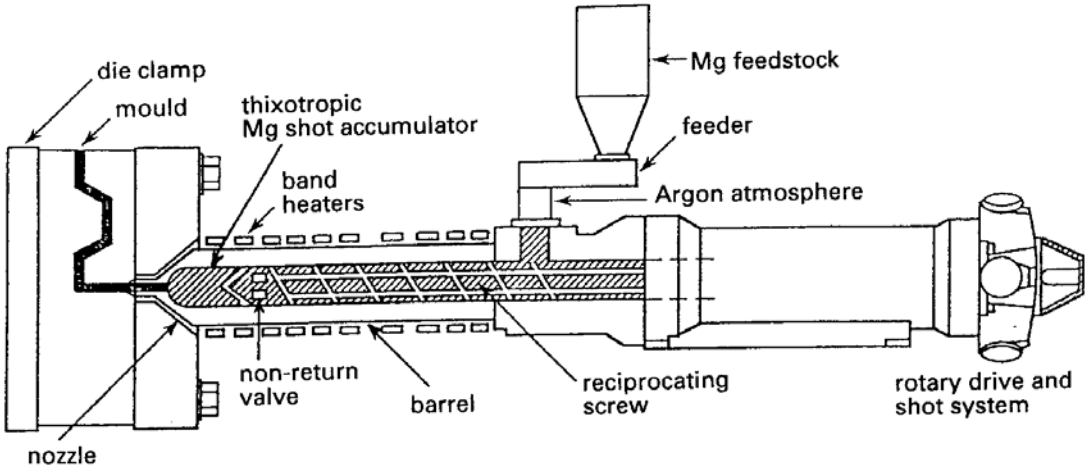

Fig. 9 Thixomolding^{R} process [35]

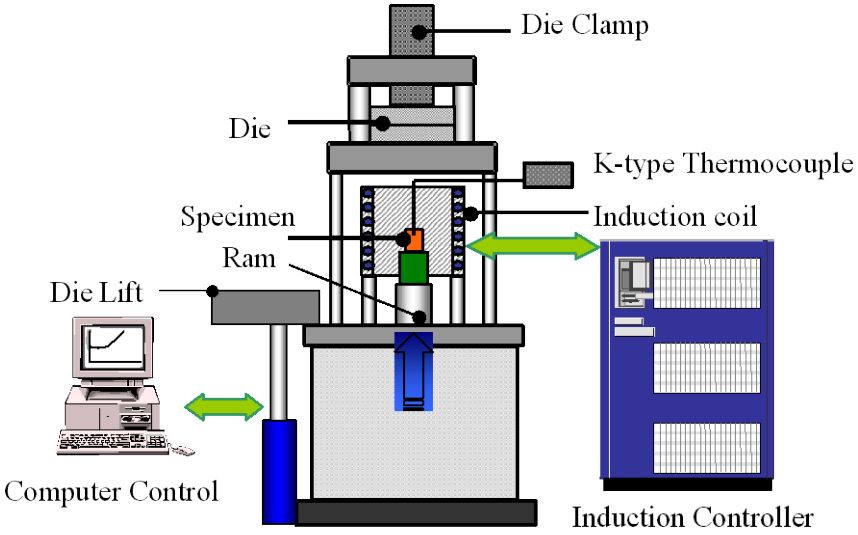

Fig. 10 Thixoforming press (courtesy University of Sheffield)

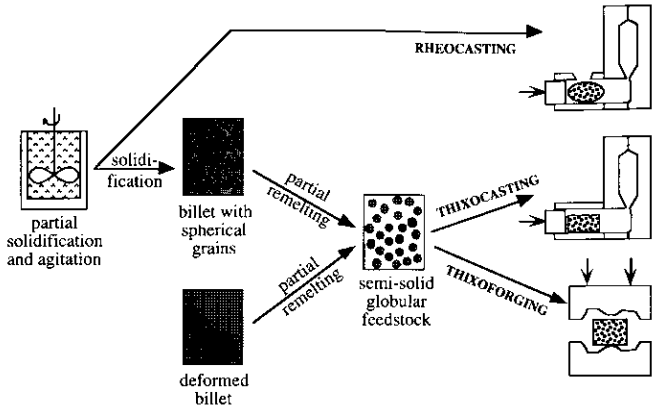

Fig.11 Schematic illustration of different routes for semisolid metal processing [40]

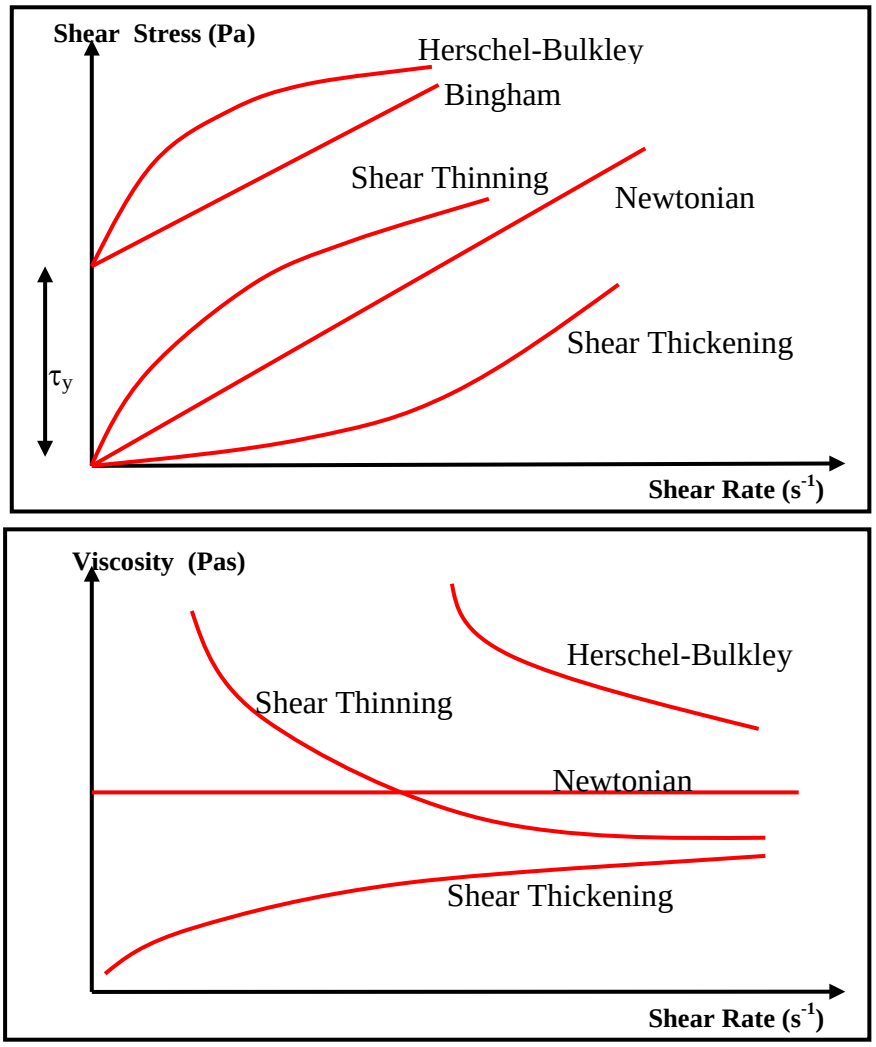

Fig. 12 Shear stress versus shear rate and associated viscosity versus shear rate curves for a variety of types of rheological behaviour

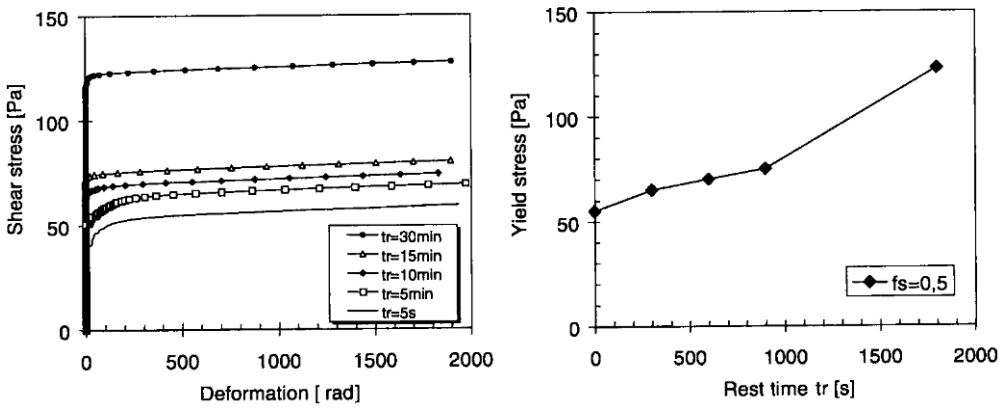

(a) (b)

Fig. 13 Shear-stress ramp experiments after different rest times (tr) for Sn-15%Pb [66]. (a) Shear stress versus deformation angle. (b) Shear stress versus rest time. Temperature 195ºC, fraction solid 0.5, globular structure prepared by shearing at $100s^{-1}$ at a cooling rate of 1ºC/min.

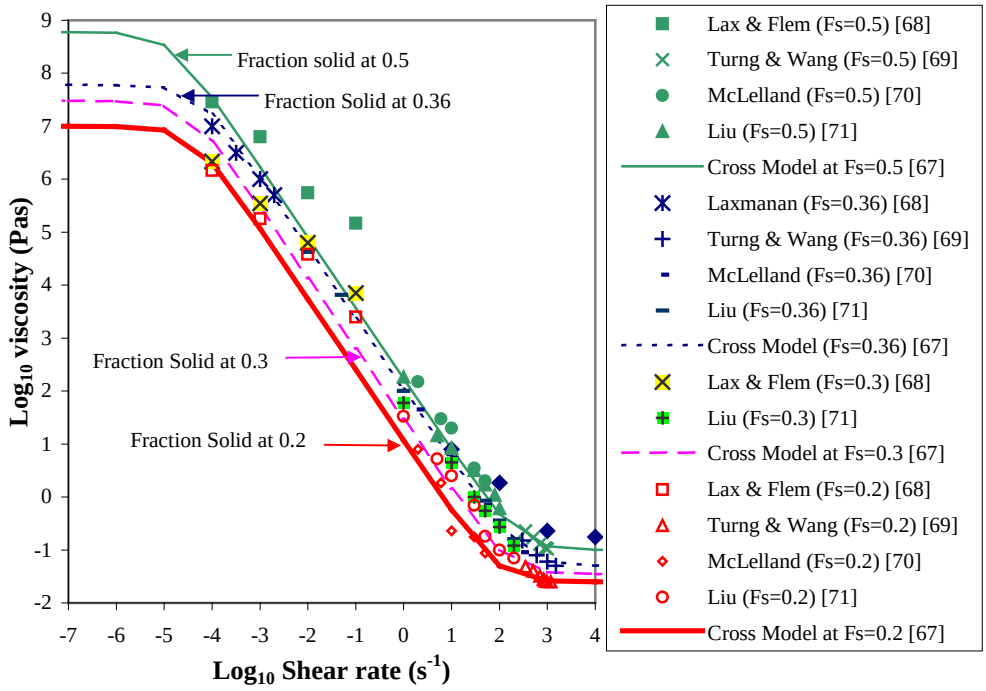

Fig. 14 Cross Model fitted to apparent viscosities obtained from various works on Sn15%Pb alloys [71]

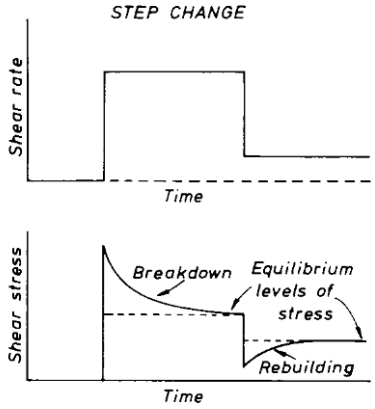

Fig. 15 Response of an inelastic thixotropic material to firstly a step-change up in shear rate and then a step-change down (after [64]).

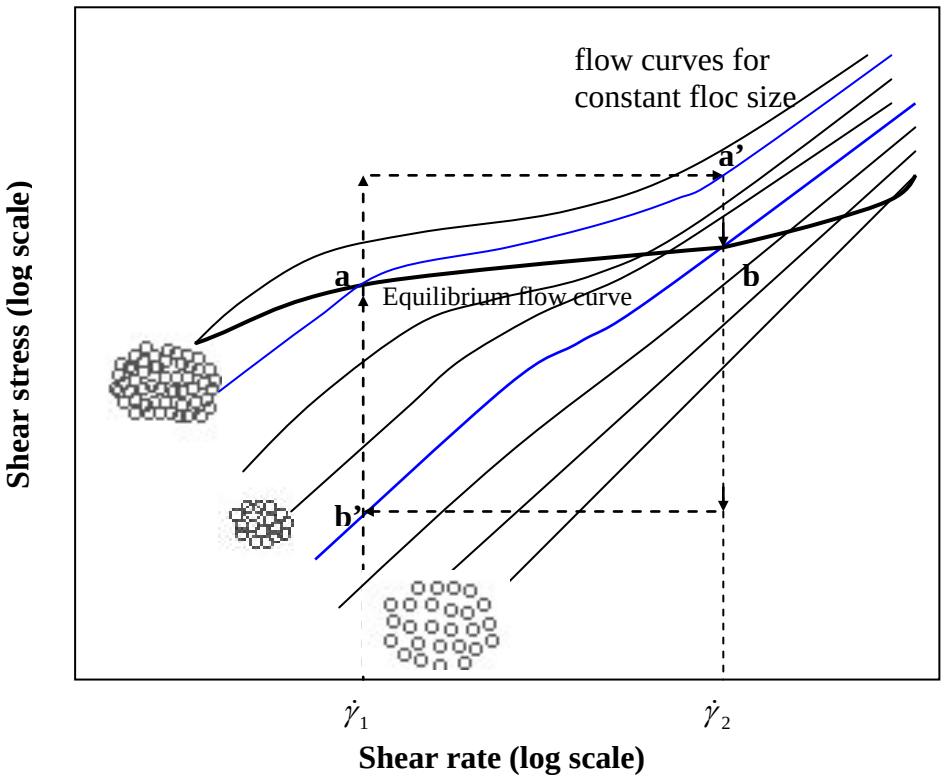

Fig. 16 Flow curves of a flocculated suspension (after [65])

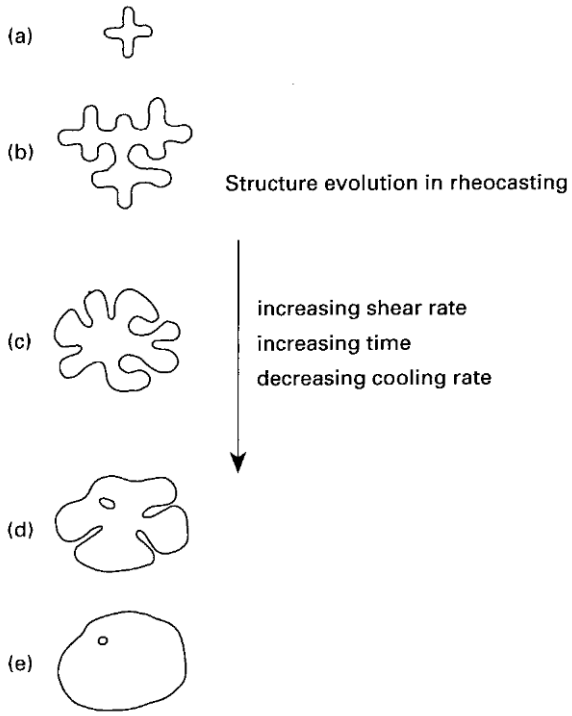

Fig. 17 Schematic illustration of evolution of structure during solidification with vigorous agitation

(a) initial dendritic fragment; (b) dendritic growth; (c) rosette; (d) ripened rosette; (e) spheroid [45]

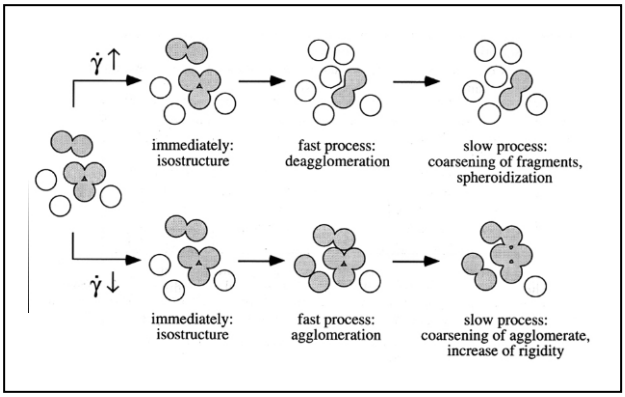

Fig.18 Schematic model describing the fast and slow processes in a semi-solid material's structure after shear rate up and down jumps (taken from ref. [47])

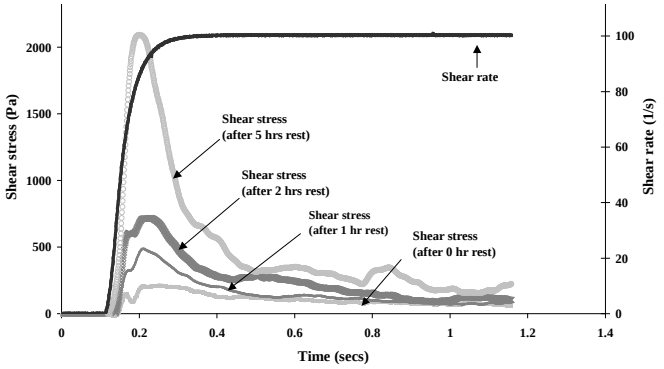

Fig. 19. Shear rate jumps from 0 to 100 s^{-1} after different rest times for Sn 15%Pb alloy at fraction solid 0.36 [86].

(a)

(b)

(c)

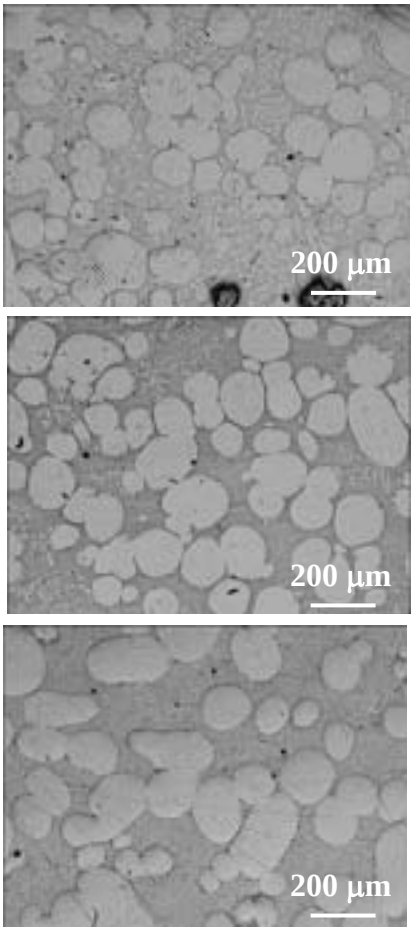

Fig.20 Microstructures of Sn 15%Pb alloy ($f_s = 0.36$) at various rest times: (a) 0 h (b) 1 h and (c) 2 h [86].

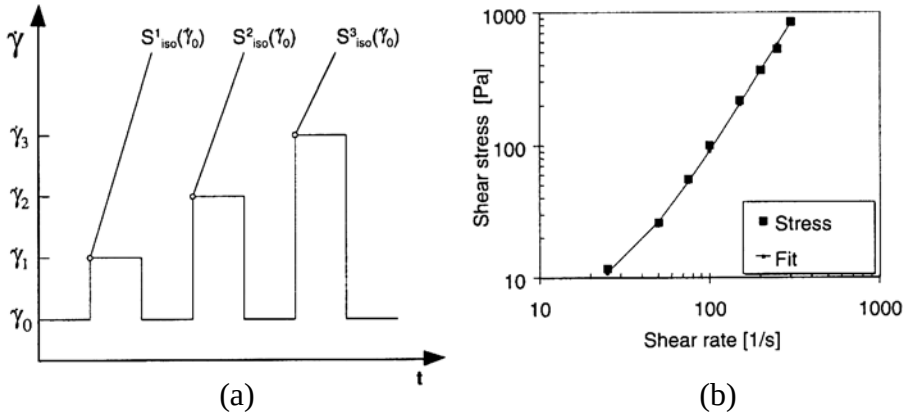

(a) (b)

Fig. 21 (a) Series of step changes in shear rate to obtain (b) isostructural flow curve [66]. The isostructural shear stress S_{iso} is measured immediately after each step up in shear rate. In between each experiment, the material was sheared at the equilibrium shear rate $\dot{\gamma}_0$ of 100s^{-1}. (Sn-15%Pb, 198ºC, $f_s = 0.41$). The exponent for the fit to (b) is 2.07 and hence the isostructural behaviour is termed shear thickening.

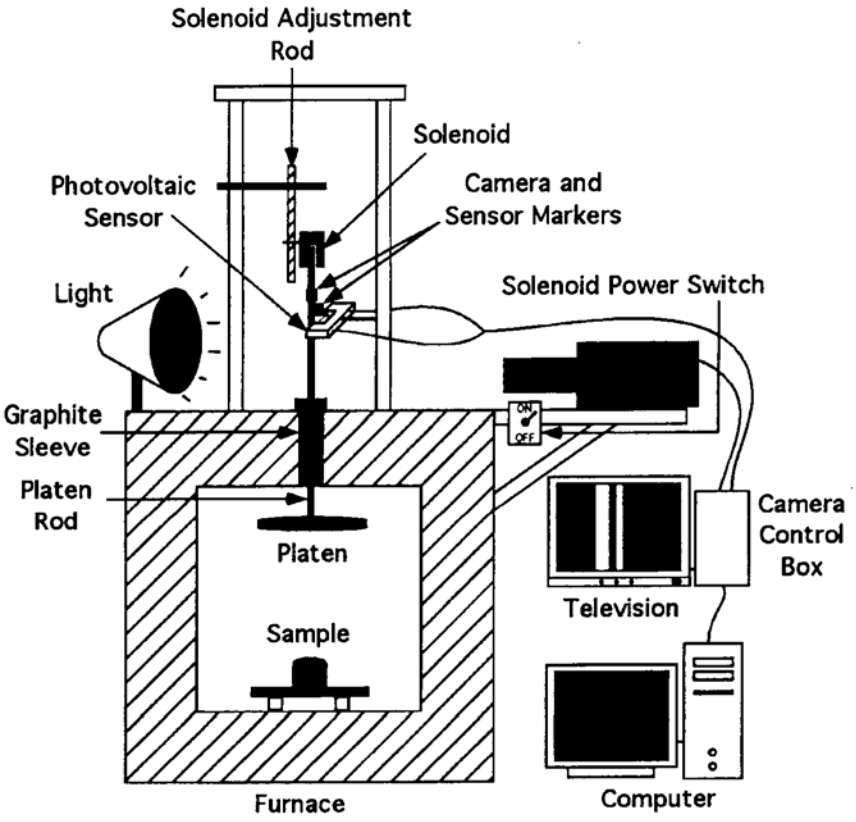

Fig. 22 Schematic of the drop forge viscometer [90].

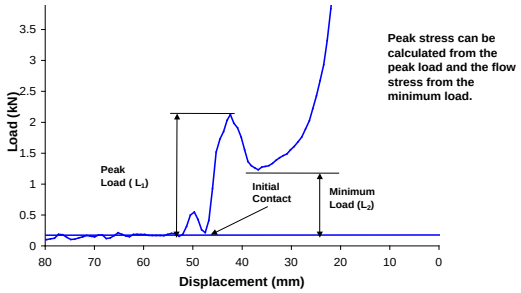

Fig. 23 Typical signal response to rapid compression of a semisolid alloy slug [91].

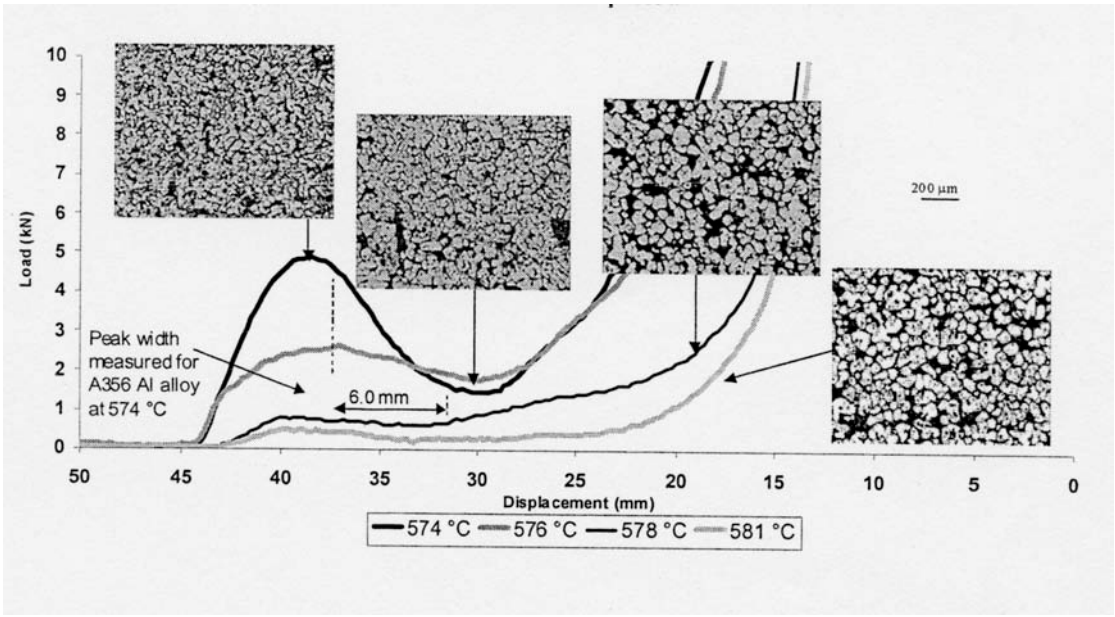

Fig. 24 Load signals and microstructures at different temperatures for Alusuisse A356 aluminium alloy in rapid compression tests (ram speed 500 mm/s, zero soak time) [91].

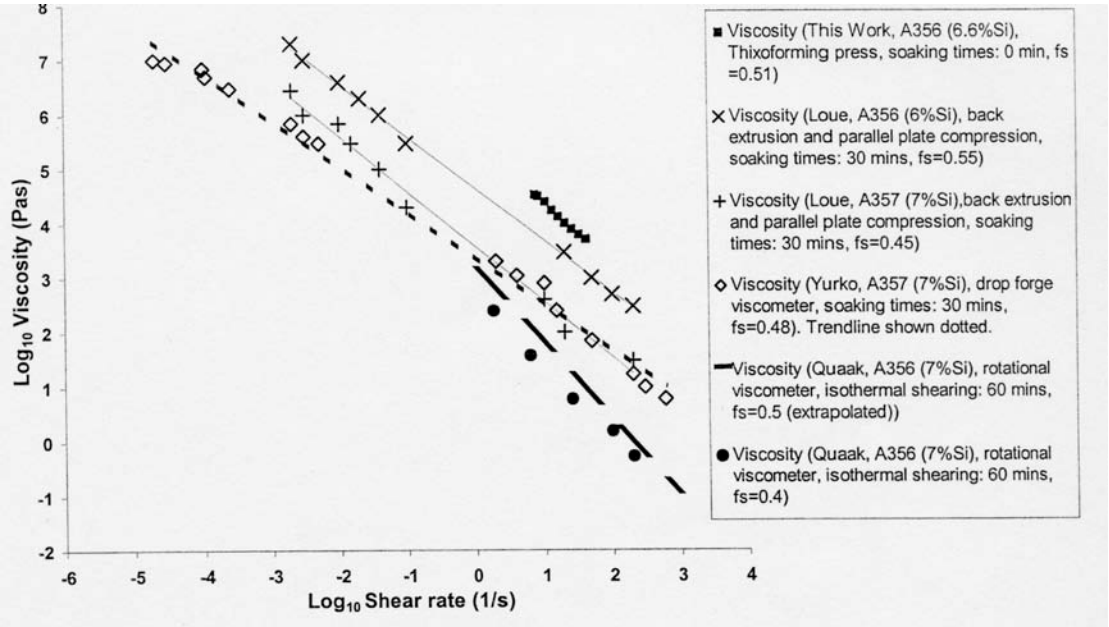

Fig. 25 Comparison of apparent viscosities obtained by various experimental techniques and conditions [91]. (‘This work’ is [91], ‘Loue’ is [89], ‘Yurko’ is [90], ‘Quaak’ is [47]).

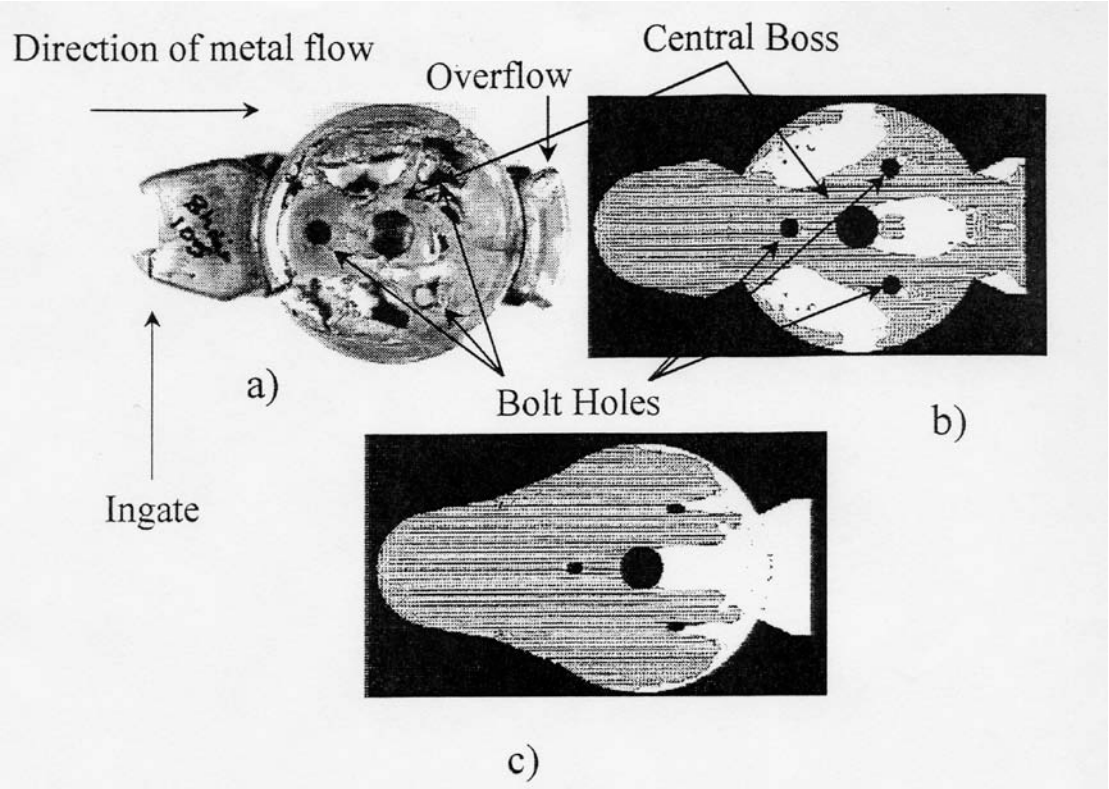

Fig. 26 Numerical simulation of die filling [93]. (a) Partial filling of die. (b) Modelling simulation of (a) where white corresponds to dark on (a). (c) Modelling simulation with improved die design showing smoother filling.

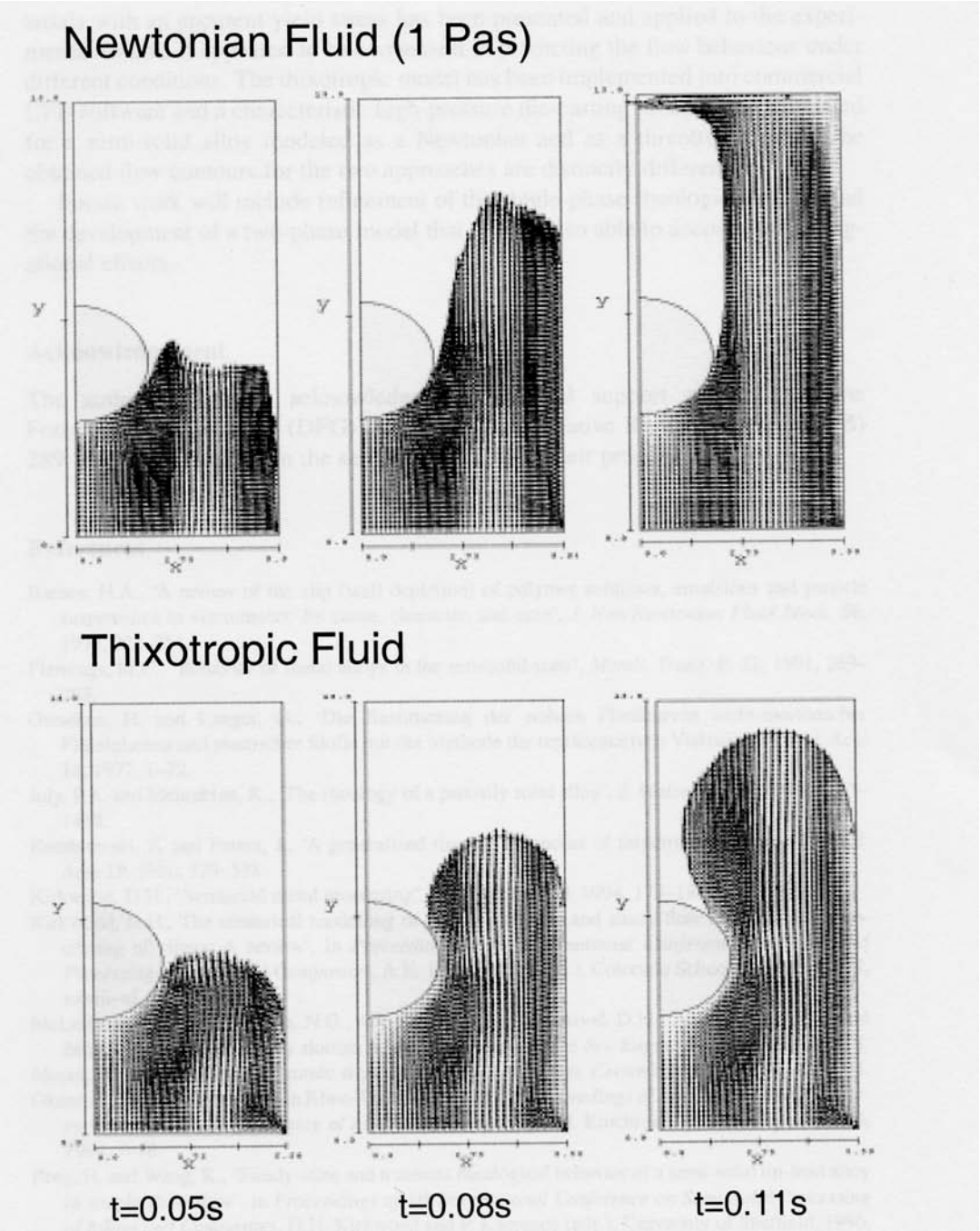

Fig. 27 Comparison between simulation of flow into a cavity with a round obstacle assuming Newtonian behaviour and assuming thixotropic behaviour [84].

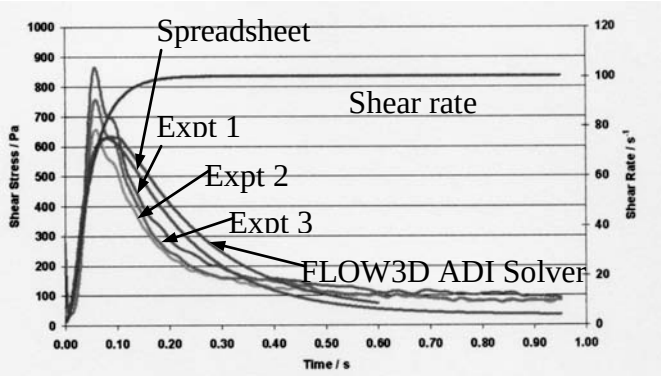

Fig. 28 Shear rate jump from 1-100 s^{-1} in SnPb alloy ($f_s = 0.36$), showing repeats of the same experiment and modelled fits using a spreadsheet and FLOW-3D [98].

Newtonian Bingham

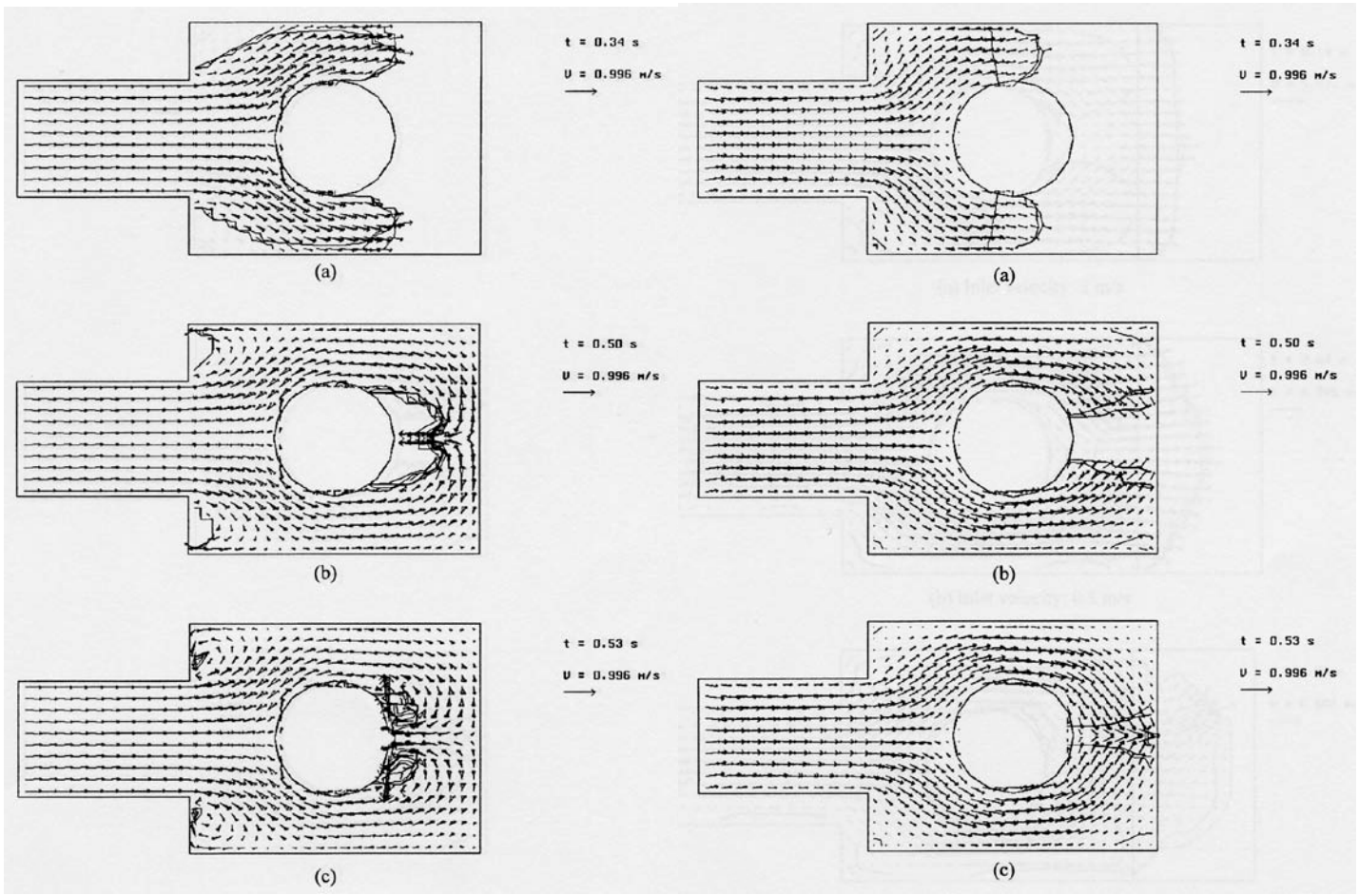

Fig. 29 Comparison of Newtonian (on the left) and Bingham (on the right) filling behaviour for a three dimensional cavity with a cylindrical obstacle [105].

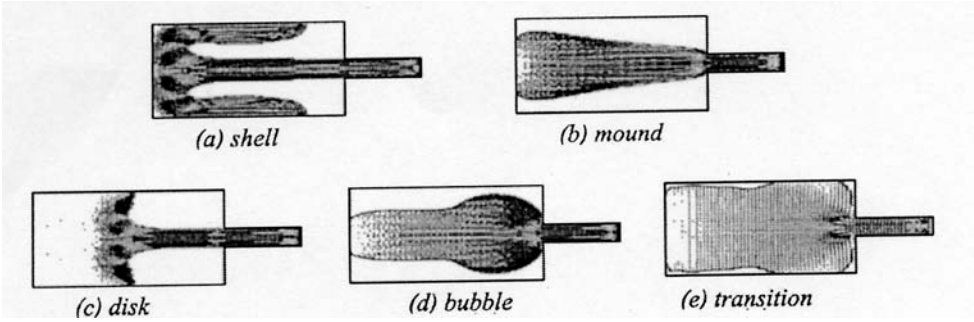

Fig. 30 Flow patterns found by modelling [107].

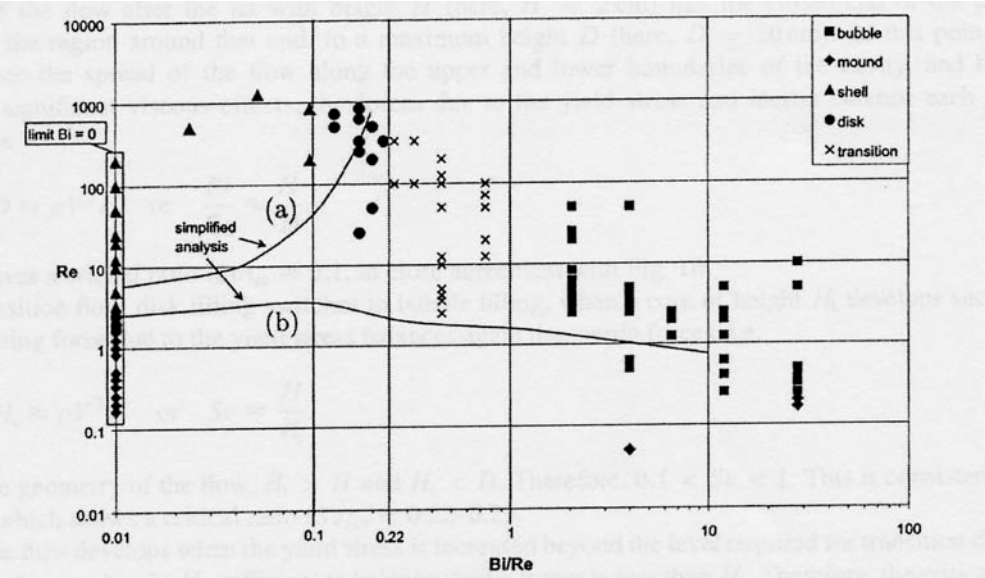

Fig. 31 Map showing flow patterns in Fig. 30 as a function of Reynolds number Re and the ration of the Bingham number to the Reynolds number (Bi/Re) [105]. Curves (a) and (b) represent simplified analyses.

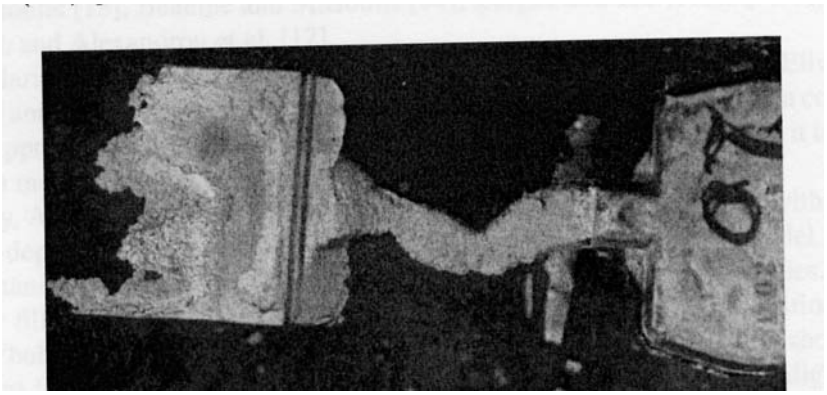

Fig. 32 Flow instability of the ‘toothpaste’ type in semisolid processing. The metal is filling from the right to the left [114].

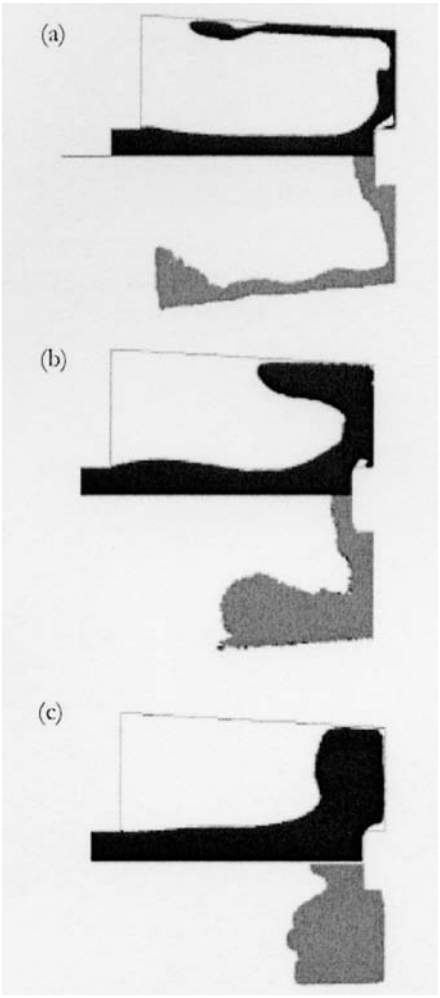

Fig. 33 Comparison between experimental and simulated filling of a cavity (initial ram velocity 0.8 ms^{-1}, diameter of tube 25mm) [115]. (a) Fraction solid 0.52. (b) Fraction solid 0.58. (c) Fraction solid 0.73. In each figure, the upper part is the simulation and the lower part the experimental result obtained with interrupted filling.

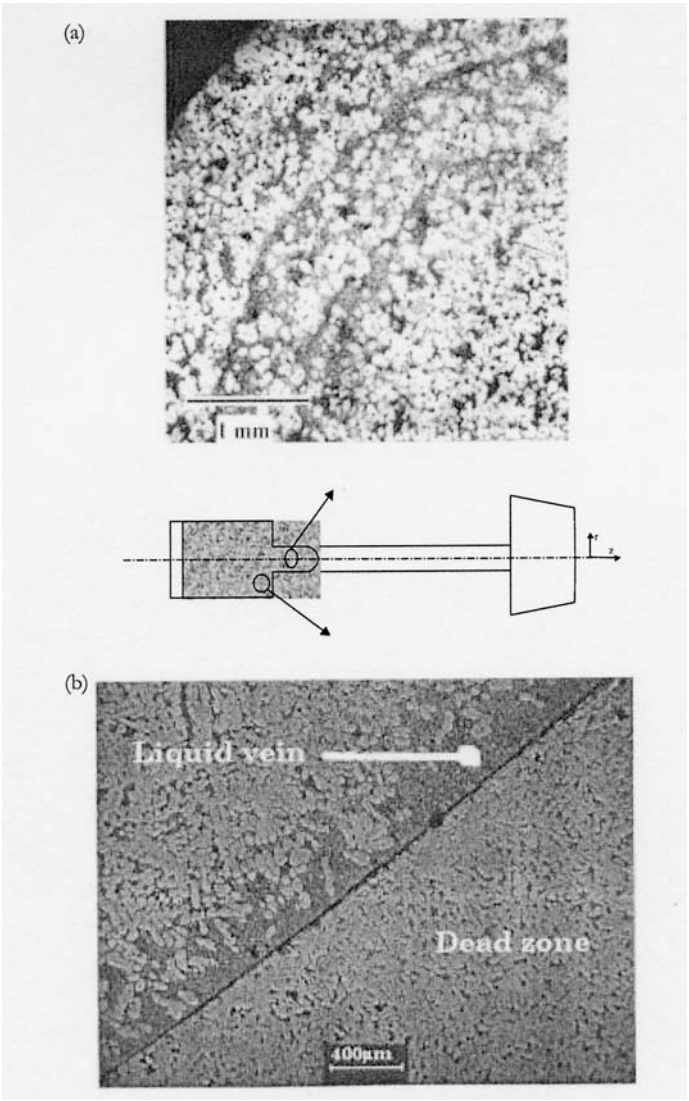

Fig. 34 (a) Cross-section through the semisolid material solidified in a tube in a Poiseuille-type experiment. The eutectic-rich concentric rings are due to veins of liquid formed in the shot sleeve. (b) shows such a vein formed at the limit of the dead zone in the shot sleeve (see inset). [115].

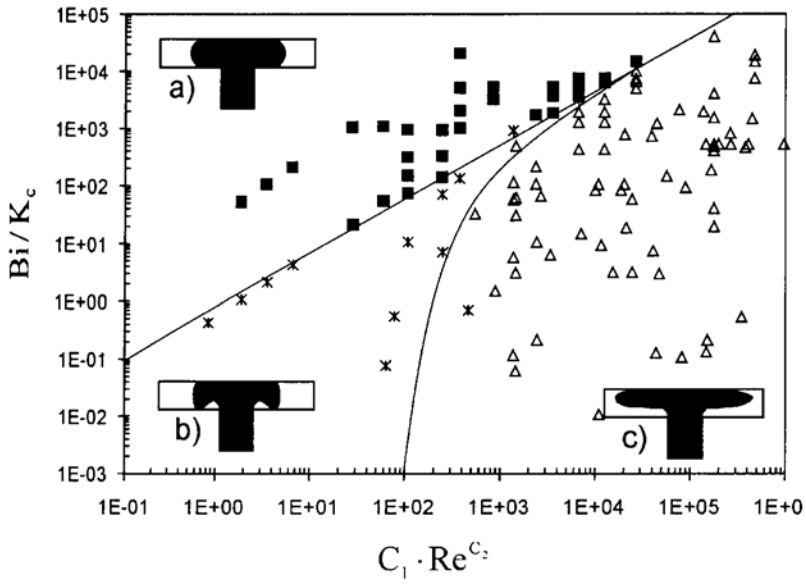

Fig. 35 Map of types of flow [124]. a) Laminar, b) Transient, c) Turbulent. Bi is the Bingham number, K_c a rheological number, C_1 , C_2 geometric constant and Re the Reynolds number. K_c, C_1 and C_2 are not specified in the paper.

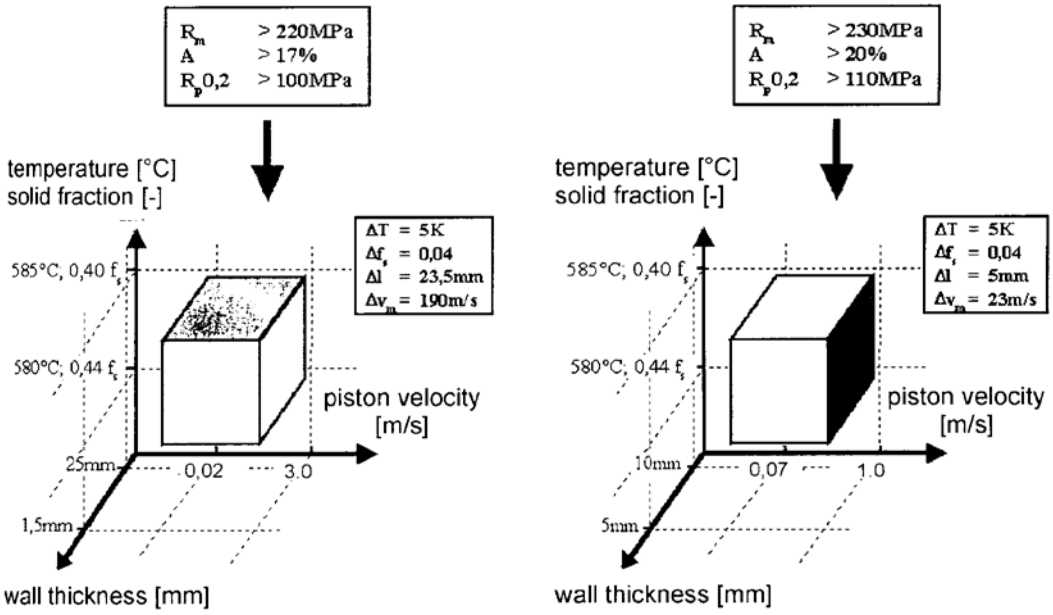

Fig. 36 Three dimensional process window for aluminium alloy A356 [124]. Mechanical properties are given in the two top boxes. The smaller boxes summarise the process parameter windows to obtain those mechanical properties (ΔT is the temperature window, Δf_s the solid fraction window, Δl the wall thickness and Δv_m). The higher the required mechanical properties, the smaller the three-dimensional process window (compare the right hand diagram with the left).

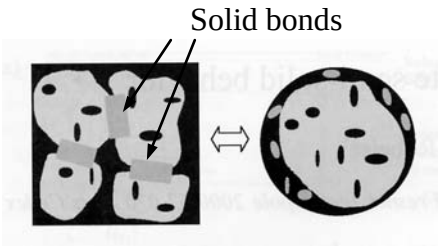

Fig. 37 Schematic representation of the semisolid microstructure with inclusions of solid and entrapped liquid surrounded by liquid and solid bonds [125].

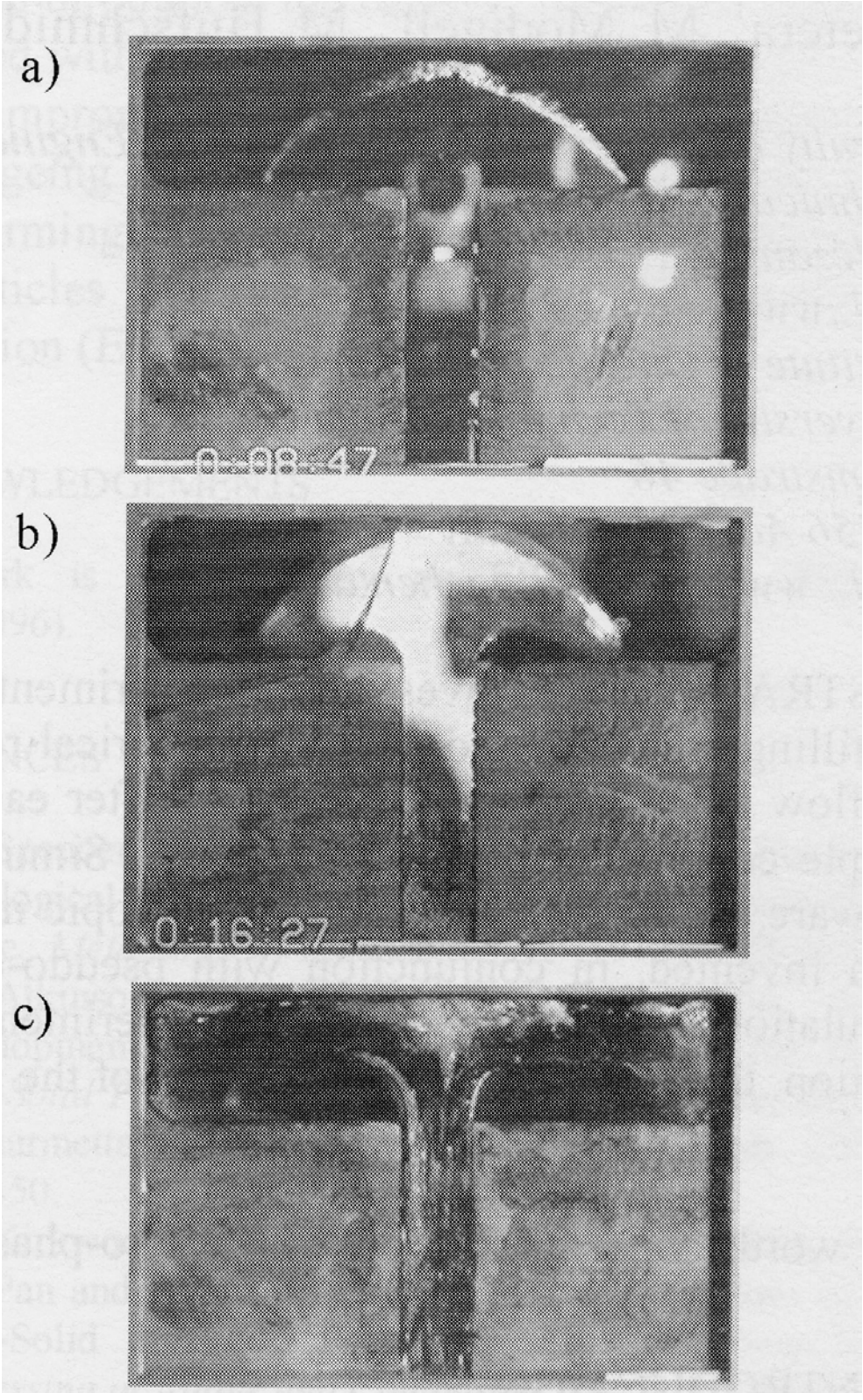

Fig. 38 Filling by Sn-12%Pb of a T-shaped cavity with a glass side showing the effect of piston velocity on the shape of the flow front [150]. Piston velocity (a) 10 mm/s (b) 50 mm/s (c) 100 mm/s.

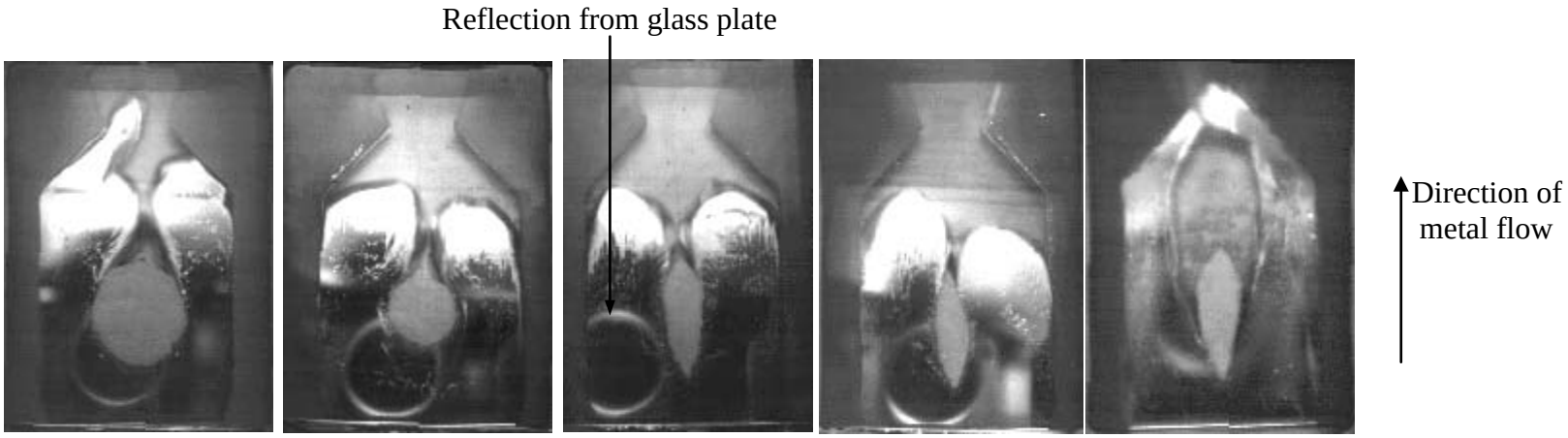

Fig. 39 Effect of obstacle size and shape on meeting of split flow fronts, Sn 15%Pb, 189^{o}C, 0.25 ms^{-1}, splayed die entrance [98]. Left to right: obstacle 30mm diameter; obstacle 20 mm diameter; experimental &, standard 'spiders' for extruding PVC pipes. Note how broader obstacle leads to flow fronts meeting with the die more full. Far right: experimental spider at 1 ms^{-1}.

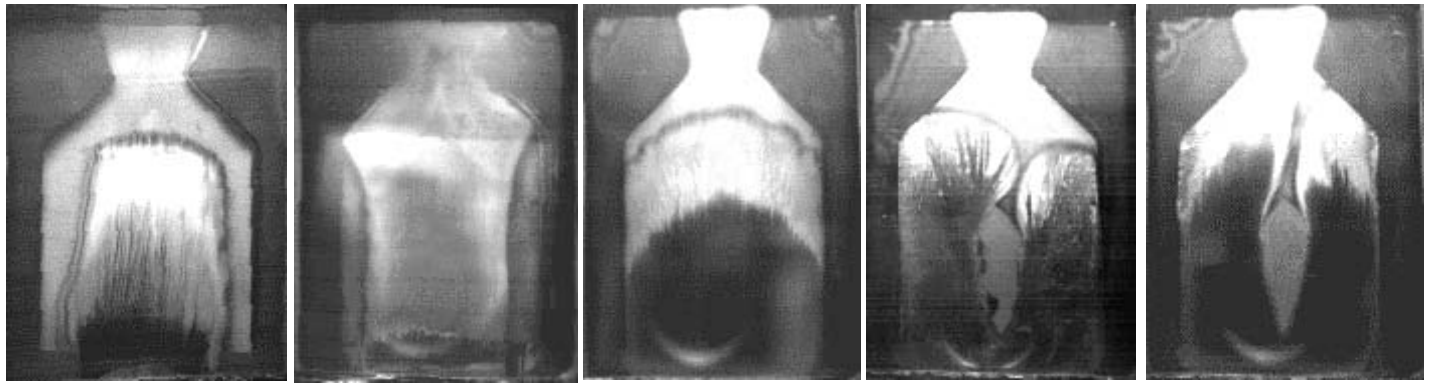

Fig. 40 Shots from filmed die filling with Al A357 [98]. Left to right: 576°C, 0.25 ms^{-1}, parallel entrance; 576°C 1ms^{-1}, parallel entrance; 1ms^{-1}splayed entrance; 0.25 ms^{-1} splayed entrance with the experimental 'spider' and the same at 1ms^{-1}, all at 577°C.